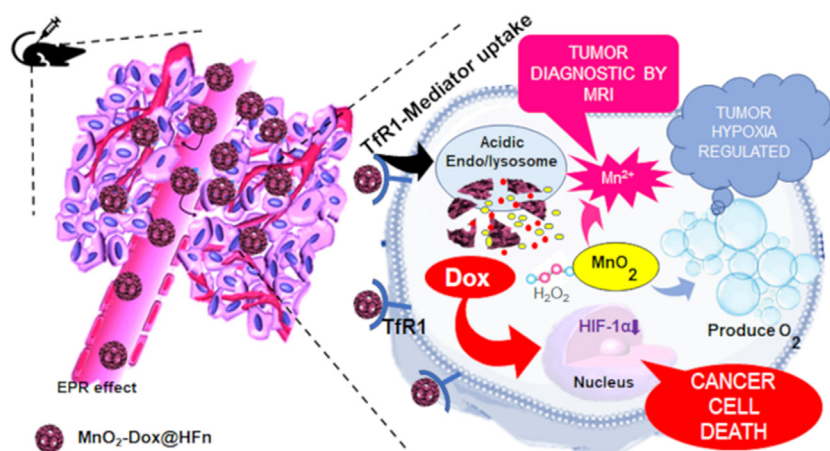Original Article

Innate tumor-targeted nanozyme overcoming tumor hypoxia for cancer theranostic use

Hanitrarimalala Veroniaina, Zhenghong Wu [*], Xiaole Qi [*]

Key Laboratory of Modern Chinese Medicines, China Pharmaceutical University, Nanjing 210009, China

GRAPHICAL ABSTRACT

ARTICLE INFO

ABSTRACT

Introduction: Hypoxic tumor microenvironment (TME) is the major contributor to cancer metastasis, resistance to chemotherapy, and recurrence of tumors. So far, no approved treatment has been available to overcome tumor hypoxia.

Objectives: The present study aimed to relieve tumor hypoxia via a nanozyme theranostic nanomaterial as well as providing magnetic resonance imaging (MRI)-guided therapy.

Methods: Manganese dioxide (MnO_2) was used for its intrinsic enzymatic activity co-loaded with the anti-cancer drug Doxorubicin (Dox) within the recombinant heavy-chain apoferritin cavity to form MnO_2-Dox@HFn. Following the synthesis of the nanomaterial, different characterizations were performed as well as its nanozyme-like ability. This nanoplatform recognizes tumor cells through the transferrin receptors 1 (TfR1) which are highly expressed on the surface of most cancer cells. The cellular uptake was confirmed by flow cytometry and fluorescence spectroscopy. *In vitro* and *in vivo* studies have been investigated to evaluate the hypoxia regulation, MRI ability and anti-tumor activity of MnO_2-Dox@HFn.

Results: Being a TME-responsive nanomaterial, MnO_2-Dox@HFn exerted both peroxidase and catalase activity that mainly produce massive oxygen and Mn^{2+} ions. Respectively, these products relieve the unfavorable tumor hypoxia and also exhibit T1-weighted MRI with a high longitudinal relaxivity of

---

33.40 mM. s^{-1}. The utility of MnO$_2$-Dox@HFn was broadened with their efficient anti-cancer activity proved both *in vitro* and *in vivo*.

Conclusions: MnO$_2$-Dox@HFn successfully overcome tumor hypoxia with double potentials enzymatic ability and diagnostic capacity. This investigation could ignite the future application for cancer theranostic nanozyme therapy.

Introduction

Tumor microenvironment (TME) is recognized jointly as the hallmark of solid tumors that is regularly featured by low levels of oxygen (hypoxia), acidosis (lysosome pH 4–5) coupled with a high concentration of reactive oxygen species (e.g., H$_2$O$_2$) [1–3]. Essentially, tumor hypoxia severely weakens cancer treatment by promoting chemotherapy resistance, tumor metastasis and tumor recurrence [4,5]. Since hypoxic cancer cells adapt their metabolism through chronic overproduction of hypoxia-inducible-factor-1 (HIF-1α) which involves multiple cellular regulations. For instance, HIF-1α regulates the up-expression of vascular endothelial protein (VEGF) which stimulates angiogenesis, resulting in proliferation and invasiveness of malignant cells [6,7]. Consequently, oxygen-carrying and oxygen-generating nanoparticles are developed to enhance tumor oxygenation since this factor seriously exacerbates cancer diagnosis and therapy [8–10]. However, most of these synthesized nanomaterials are limiting by the lower and short-time capacity to produce oxygen (O$_2$), thus any effect impacts the tumor invasion. Using TME-abundant metabolite (H$_2$O$_2$ and H$^+$) as a substrate is a valuable strategy to provide massive and continuous O$_2$ production as well as regulating this unfavorable TME [11–13]. Therefore, exploiting the intrinsic catalytic ability of manganese dioxide (MnO$_2$) via the conversion of endogenous H$_2$O$_2$ to generate O$_2$ has been conceived as one of the most effective O$_2$-generating methods [14–16]. Particularly under acidic conditions, MnO$_2$ not only acting as a catalyst but also as a reactant to produce Mn^{2+} ions. The resulting Mn^{2+} ions can improve the proton relaxation rate to achieve T1-weighted magnetic resonance imaging (MRI) for specific tumor diagnosis [17,18]. MRI is amongst the useful clinical diagnostic methods for the imaging of soft tissue, especially at early-stage tumors, as it can penetrate deeply and identify tumor lesions with high resolution [19]. Furthermore, the utilization of Mn^{2+} as an MRI contrast agent is unhazardous because Mn is one of the trace minerals required by the organism. Also, the innocuous Mn^{2+} ions are water-soluble and simply excreted by the kidneys [11] this means no fear of long-term toxicity risk when used for *in vivo* applications.

Owning all of those abilities, MnO$_2$ has been recently brought into tumor cells with various matrices, either directly as MnO$_2$ nanostructures or loaded into nanocarriers [13,15,16]. A wide range of nanocarriers have been used to deliver MnO$_2$ to the tumor site, such as PAMAM dendrimer [20] hyaluronic acid [21] cancer cell membrane [22] and mesoporous silica nanoparticle [23]. However, inorganic nanocarriers are often struggled to meet clinical expectations because they may cause an inflammatory response or neurotoxic reactions [24]. Additionally, most carriers need additional ligand functionalization to target tumor cells, they face a number of issues such as reproducibility, surface characterization and immune reactions [25]. Therefore, the use of endogenous vehicles already presents in the body like apoferritin, an empty shell of ferritin protein, which possesses a great innate active targeting ability toward tumors would be a shorter alternative route to deliver MnO$_2$ safely.

The inner surface of the recombinant heavy-chain apoferritin (HFn) has a high negative charge density which could serve as a suitable vehicle for the positively charged MnO$_2$. As being ubiquitous found in all living organisms, the potentiality of HFn to be used as a tumor-targeted nanocarrier has been widely explored. First, the inner cavity of HFn is large enough to accumulate MnO$_2$ with an outer diameter of ~12 nm, making it ideal for passive tumor targeting through enhanced permeability and retention (EPR) effect [26]. The remarkable flexibility of the HFn protein shell also allows its use as an excellent drug delivery carrier which may encapsulate larger compounds than its size [27]. Second, the protein structure is a hollow nanocage composed of 24 self-assembling subunits that decay under an acidic pH and recombine in a neutral environment, promising TME selective drug delivery [28]. Naturally, HFn binds specifically to transferrin receptors 1 (TfR1) via clathrin-coated pits to be internalized within the cancer cells [29]. It is well-known that TfR1 are highly expressed by > 100-fold on the surface of most common cancer cells due to their increased iron demand compared to normal cells [30,31]. TfR1 has therefore been advised as a privileged targeting marker for the tumor-selective delivery to increase the accumulation of nanomaterial in the tumor site and minify the side effects on normal tissues [32]. Recently, nanozyme has spawned larger advances in nanotechnology research. Outline that nanozyme are small nanomaterials between 1 and 100 nm size owning enzymatic-like properties [33]. Taken together, nanozyme-based theranostic material could be a better alternative to treat cancer especially by modulating the unfavorable TME.

In the present work, a versatile theranostic nanozyme material in which MnO$_2$ and Doxorubicin (Dox) were co-loaded within the HFn nanocage to form MnO$_2$-Dox@HFn was designed for the first time.

Experimental

Synthesis of MnO$_2$-Dox@HFn

MnO$_2$ was formed by a simple redox reaction between potassium permanganate (KMnO$_4$) and poly-allylamine hydrochloride (PAH). Shortly, 80 μL of KMnO$_4$ (10 mg mL^{-1}) was added in 20 mL deionized water and 80 μL PAH (23.6 mg mL^{-1}) under moderate stirring at 37 °C to allow MnO$_2$ growth. After 30 min reaction, the MnO$_2$ solution was centrifuged and the precipitate was collected in 2 mL deionized water, MnO$_2$ was obtained. To disassemble the HFn subunits, the pH of the solution was lowered to 3.5 by adding 0.1 M HCl. Then, MnO$_2$ (6.64 mM) and Dox (1.5 mM) were added to the protein solution (10 mg mL^{-1}), the molar ratio of MnO$_2$: Dox: HFn was set as 1:2:5. The mixture was stirred for 15 min and the pH was finally adjusted to 7.4 using 0.1 M NaCl to allow the self-assembly of the HFn nanocage. The resulting solution was stirred for an additional 2 h at room temperature. To remove the unloaded molecules, the mixture was dialyzed against a storage buffer for 24 h. The supernatant was analyzed on a Sephadex 100 column for size-exclusion chromatography (SEC). The fraction volume was set at 1 mL, and the absorbance of each eluted fraction was recorded at 280, 370 and 480 nm by UV spectra.

Enzymatic activity

The production of Mn^{2+} in the tubes containing MnO_2-Dox@HFn under different pH (7.4, 6.5 and 5.0) with or without the presence of 100 μM H_2O_2 was investigated. To assay the O_2 generation from varied concentrations of MnO_2-Dox@HFn, [Ru(dpp)3]Cl_2 was used as an O_2 sensing probe. Furthermore, MnO_2-Dox@HFn was incubated in PBS solution pH 5.0 adding 100 uM H_2O_2 to mimic the TME. After 30 min, the O_2 bubble generation was examined macroscopically. While, the peroxidase-like activity of MnO_2-Dox@HFn was measured through the catalytic oxidization of 3,3′,5,5′-tetramethylbenzidine (TMB) with H_2O_2. The experiment was performed using TMB (5 μM) and MnO_2-Dox@HFn (MnO_2 = 45 μM) in a reaction volume of 3 mL buffer solution (100 mM acetate buffer, pH 5.0) with 100 μM H_2O_2. The reaction solution was detected using the UV–vis spectra at λ = 650 nm. Additionally, the kinetic data were obtained by varying the concentrations of H_2O_2 (5, 10, 25, 50 mM) and then calculated based on the Michaelis Menten and the Lineweaver–Burk plot method.

MRI in vitro

To determine the proton relaxation rates (r1) of MnO_2-Dox@HFn, the longitudinal relaxation time T1 (s) has been investigated under different concentrations at pH 6.0 and pH 7.4. The r1 was determined as the slope of the concentration-dependent longitudinal relaxation time T1 curve.

In vitro cytotoxicity

The human cervical cancer cells (HeLa), human ovarian cancer cells (SKOV3) and 4 T1 murine breast cancer cells (4 T1) were originally obtained from the American Type Culture Collection (ATCC) and cultured with the recommended medium at 37 °C within 5% CO_2 atmosphere.

In vitro cell viability was determined by standard 3-(4,5-dimethylthiazol-2-yl)-2,5-diphenyl-tetrazolium bromide (MTT) assay after 48 h incubation under normal and hypoxic environment. A fresh medium containing $CoCl_2$ (100 μM) was used to mimic hypoxia. The half-maximal inhibitory concentration (IC_{50}) values were calculated on HeLa, 4 T1 and SKOV3 cancer cells.

Cellular uptake

To visualize the cellular uptake of the nanozyme, the surface of the protein carrier was labeled with fluorescein-5-maleimide (FAM) as previously conducted [34].

Flow cytometry was performed to analyze quantitatively the cellular uptake of MnO_2-Dox@HFn. HeLa was used as TfR1-positive cells which overexpressed TfR1, while SKOV-3 as TfR1-negative cells which have lower TfR1 expression levels. Cells were co-incubated with FAM-MnO_2-Dox@HFn for different times (1, 2, and 4 h). After washes with cold PBS, cells were collected by trypsinization, and then analyzed immediately. To study the interaction and endocytosis mechanism between cancer cells and MnO_2-Dox@HFn nanomaterials, HeLa cells were seeded into six-well plates (5 × 10^4 cells per well). Firstly, for the analysis of energy-dependent mechanism: the cells were divided into three groups; the control group was co-cultivated directly with FAM-MnO_2-Dox@HFn (1.5 mg mL^{-1}) at 37 °C for 2 h; the second group of cells was co-cultured with the above nanomaterial at 4 °C for 2 h (low temperature inhibits cell physiology and metabolic activity) and the third group of cells was pretreated with sodium azide (1 mg mL^{-1}) for 1 h (sodium azide inhibits intracellular ATP synthesis), followed by incubation of FAM-MnO_2-Dox@HFn for 2 h. Secondly, for the endocytosis mechanism analysis: cells were pre-treated with endocytic inhibitors, including chlorpromazine (8.5 μg mL^{-1}), genistein (56.75 μg mL^{-1}) and amiloride (133 μg mL^{-1}) for 1 h prior to FAM-MnO_2-Dox@HFn (1.5 mg mL^{-1}) administration and further incubated for 2 h [35]. Quantitative analysis by flow cytometry was carried out using the above-mentioned method. Compared with the control cells without inhibitors, the decrease in the uptake rate in the presence of inhibitors demonstrated the corresponding endocytosis pathways. Besides, the qualitative intracellular uptake of FAM-MnO_2-Dox@HFn was monitored by confocal laser scanning microscopy (CLSM).

Cellular hypoxia amelioration

The intracellular O_2 generation of MnO_2-Dox@HFn was investigated by using [Ru(dpp)3]Cl_2 fluorescence. HeLa cells were ventilated with nitrogen for 3 h first to induce severe hypoxia. Then incubated with MnO_2-Dox@HFn (10 μg mL^{-1}) for 3, 6, 12 and 24 h and further incubated with 1 μM [Ru(dpp)3]Cl_2 for 4 h to assay the O_2 content. Finally, cells were rinsed and treated with 4% paraformaldehyde for CLSM imaging.

Western blot analysis

HeLa cells were incubated with $CoCl_2$ (100 μM) to induce severe hypoxia since $CoCl_2$ inhibits PHD enzyme which degrades HIF-1α [36]. After 48 h incubation with different formulations, HIF-1α expression was assessed by western blot (WB) as previously conducted [5].

Ethics statement

All experiments involving animals were conducted according to the ethical policies and regulations provided by the Guide for Care and Use of Laboratory Animals, approved by China Pharmaceutical University (Approval no. 2019-1205).

In vivo study

Female Balb/c mice weighing 18–20 g were used and the tumor-bearing Balb/c mice model was established by subcutaneously injecting 4 T1 tumor cells (1 × 10^6 cells suspended in 100 μL of saline) into the right flank breast of each mouse. The experiment was performed when the tumor volume reached ≈200 mm^3.

MRI in vivo imaging

A clinical MRI scanner was used to observe MR imaging. Intratumor, intramuscular, and intravenous (via tail vein) injection of MnO_2-Dox@HFn (0.2 mM MnO_2) was embarked. T1-weighted imaging was done with the following parameters: TR = 760 ms; TE = 16.9 ms; field of view = 100 cm^2; matrix: 256 mm × 256 mm; slice thickness = 3 mm and space = 0.5 mm.

In vivo Anti-tumor activity

The mice were randomly divided into five groups (n = 3) and treated intravenously with different formulations. The doses of MnO_2 and Dox were kept at 2.5 mg kg^{-1} and 2.5 mg kg^{-1}, respectively, in those groups and the treatment was studied for 10 days.

To evaluate the apoptotic response in tumor tissues, terminal deoxynucleotidyl transferase dUTP-biotin nick end labeling (TUNEL) staining and hematoxylin and eosin (H&E) staining was conducted. The hypoxia in tumor tissues was analyzed through the expression of HIF-1α protein by immunohistochemistry. More-

over, staining for the Ki-67 antigen was used to evaluate the tumor cell proliferation.

Statistical analysis

Data are presented as mean ± standard deviation (SD) of the mean for results obtained from three independent trials unless otherwise indicated. Student's *t*-test (two-tailed) or analysis of variance (ANOVA) was used to determine statistical significance between two or more groups, respectively. The results of p-values < 0.05 were considered statistically significant.

Results and discussion

Synthesis and characterization of MnO_2-Dox@HFn

The production of recombinant human HFn from *E. coli* ended up with 30 mg L^{-1} protein. The purification of HFn was revealed via SDS-PAGE (**S1**, Supplementary material). In the effluent eluted by 300 mM Imidazole, high purity protein subunits were observed at the band 29 kDa, in line with the molecular weight of the recombinant HFn monomer [37]. Protein determination at 280 nm by Nanodrop displayed only one peak of protein (**S2**), confirming the successful purification of HFn. Spherical cage-like was observed through TEM analysis of HFn in **S3**, with a mean size diameter of 12.05 ± 1.3 nm.

MnO_2 and Dox were loaded into the HFn protein cavity by the easiest pH change method. The SEC profile showed the co-elution of the protein nanocage, MnO_2 and Dox in fraction 4 (Fig. 1A), suggesting the combination of MnO_2-Dox@HFn nanomaterial. The SDS-PAGE of various formulations revealed a similar band at MW ~ 29 kDa, as did the blank HFn (Fig. 1B), showing that encapsulation of the molecules had no impact on the HFn subunit structure. Correlate with this result, the native PAGE of MnO_2-Dox@HFn also displayed an identical band to that of HFn alone, indicating that the HFn nanocage retained its structural integrity and was unaltered during the core loading (**S4**). Additionally, HFn and MnO_2-Dox@HFn exhibited a similar CD spectrum in Fig. 1C, indicating that the secondary structure of the protein did not change after mineralization. According to the UV–vis spectra of the MnO_2-Dox@HFn synthesis, the typical peak of $KMnO_4$ (~525 nm) has disappeared and a new visible absorption at ~370 nm was observed, attributed to the formation of MnO_2 (Fig. 1D). The emerging peaks at 280 nm, 370 nm, and 480 nm highlighted the presence of HFn protein, MnO_2, and Dox, respectively. Furthermore, the full XPS of MnO_2-Dox@HFn indicated the presence of spectrum C, O, N, and Mn elements in Fig. 1E. Notably, the Mn 2p spectrum defined two peaks centered at 653.8 eV and 642.0 eV (Fig. 1F), corresponding respectively to Mn $2p_{1/2}$ and Mn $2p_{3/2}$, characteristic of MnO_2. The spin energy separation of 11.8 eV indicated that the oxidation state of Mn was mainly + 4 [16]. No signal of Mn_2O_3 (641 eV) nor $KMnO_4$ (647 eV) were observed in the XPS spectra, further confirming that the present MnO_2 is in the 4 + oxidation state. Mn concentration in MnO_2-Dox@HFn was quantified by ICP-AES and found to be 0.4 mM. A similar Dox loaded rate of 48.4% was achieved as evaluated by the calibration curve (**S5**). Indeed, the encapsulation of Dox into HFn nanocages depends on their electrostatic interactions. The conjugation of the hydrophobic Dox to the N-terminus of HFn protein is expected to result in a self-assembly behavior. Because the pKa of Dox is 8.3, it can easily be attached to the negatively charged internal surface of HFn in the mildly acidic loading buffer. Besides, the protein surface charge of blank HFn shifted from −14.99 ± 2.65 mV to −21.02 ± 1.37 mV after MnO_2 loading (Fig. 1G), indicating the electrostatic interaction between HFn and MnO_2 conjugation. The Mn atom basic unit of MnO_2 could

be linked to the O atoms of the amino acid of HFn protein via an intermolecular hydrogen bonding [38]. Furthermore, the positive charge of MnO_2 (31.19 ± 2.05 mV) was hidden when it's encapsulated within the MnO_2-Dox@HFn nanozyme (−24.68 ± 1.58 mV). According to TEM, MnO_2-Dox@HFn was found to be uniform with an external diameter of 10 ~ 12 nm (Fig. 1H), a perfect size to exhibit strong catalytic activity [33]. Fig. 1I shows that MnO_2-Dox@HFn dispersed well without any obvious aggregation in PBS, physiological saline, FBS and DMEM, with polydispersity lower than 0.3. The results suggest that MnO_2-Dox@HFn was stable in physiological circumstances and suitable for intravenous administration. Both blank HFn and MnO_2-Dox@HFn in FBS and DMEM medium possess a mean hydrodynamic diameter around 13 nm with a negative zeta potential charge (**S6**), which further proved the stability of the nanoparticles. Eventually, negligible particle size fluctuations were observed between the MnO_2-Dox@HFn stored for 4 weeks and the freshly prepared material (**S7**), confirming their long-term stability.

TME-response payload release

The drug release behavior of Dox from MnO_2-Dox@HFn was quantified by UV–vis spectrophotometer and the particle size were measured to monitor the disintegration of the nanozyme. As seen in Fig. 2A, differences in solution pH can lead to variance in the drug release behavior. At pH 7.4, no significant release of Dox was observed within 48 h and the particle size

was fairly stable (**S8**). Contrarily under acidic pH, a burst release occurred in the first six hours due to the dissociation of the MnO_2-Dox@HFn system, which was confirmed by the increase in particle size to 154.62 ± 1.57 nm at pH 5.0. This result is consistent with the previous report due to the HFn nanoshell disintegration under an acidic environment [34]. To evaluate the Dox release mechanism of MnO_2-Dox@HFn, the cumulative release profile was fitted to the five kinetic equations [39]. The Korsmeyer-Peppas model was found to represent the kinetics of drug release from MnO_2-Dox@HFn (Table S1). This model provides further information on the value of release exponent 'n', which was<0.4, indicating that the release mechanism could be described as a Fickian diffusion mechanism [39]. Simultaneously, the degradation behavior of MnO_2 in MnO_2-Dox@HFn was investigated by quantifying the release of Mn using AAS under various solutions to mimic TME. It can be seen in Fig. 2B that MnO_2 was degraded rapidly at pH 5.0 and pH 6.5, particularly in the presence of H_2O_2. These results confirmed the ultrasensitive response of MnO_2-Dox@HFn to pH and H_2O_2, characteristic of TME.

Enzymatic activity

It is well known that MnO_2 possesses intrinsic catalytic activity and produce colorless Mn^{2+} ions in the mildly acidic environment. Considering this fact, MnO_2-Dox@HFn was placed under different pH solutions with or without the presence of H_2O_2. After 3 h, it was found that at pH 6.5 and pH 5.0 in presence of H_2O_2, the solution was becoming colorless (**S9**). This result demonstrates the reactivity of MnO_2-Dox@HFn nanozyme in an acidic H_2O_2 condition that induces the production of uncolored Mn^{2+} ions. Besides, the catalytic O_2 generation of MnO_2-Dox@HFn was monitored using [Ru(dpp)3]Cl_2, an O_2 detector sensor that reduced its luminescence by molecular O_2 [40]. As shown in Fig. 2C, [Ru(dpp)3] Cl_2 was gradually quenched as the concentration of MnO_2-Dox@HFn increases due to the generation of O_2, in accordance with the previous report [41]. Notably, once located in the cancer cell, intact MnO_2-Dox@HFn can exert catalase activity since H_2O_2 could diffuse into the HFn cavity through the hydrophilic channels and interacts with the contained MnO_2 [32]. Nevertheless, oxygen bub-
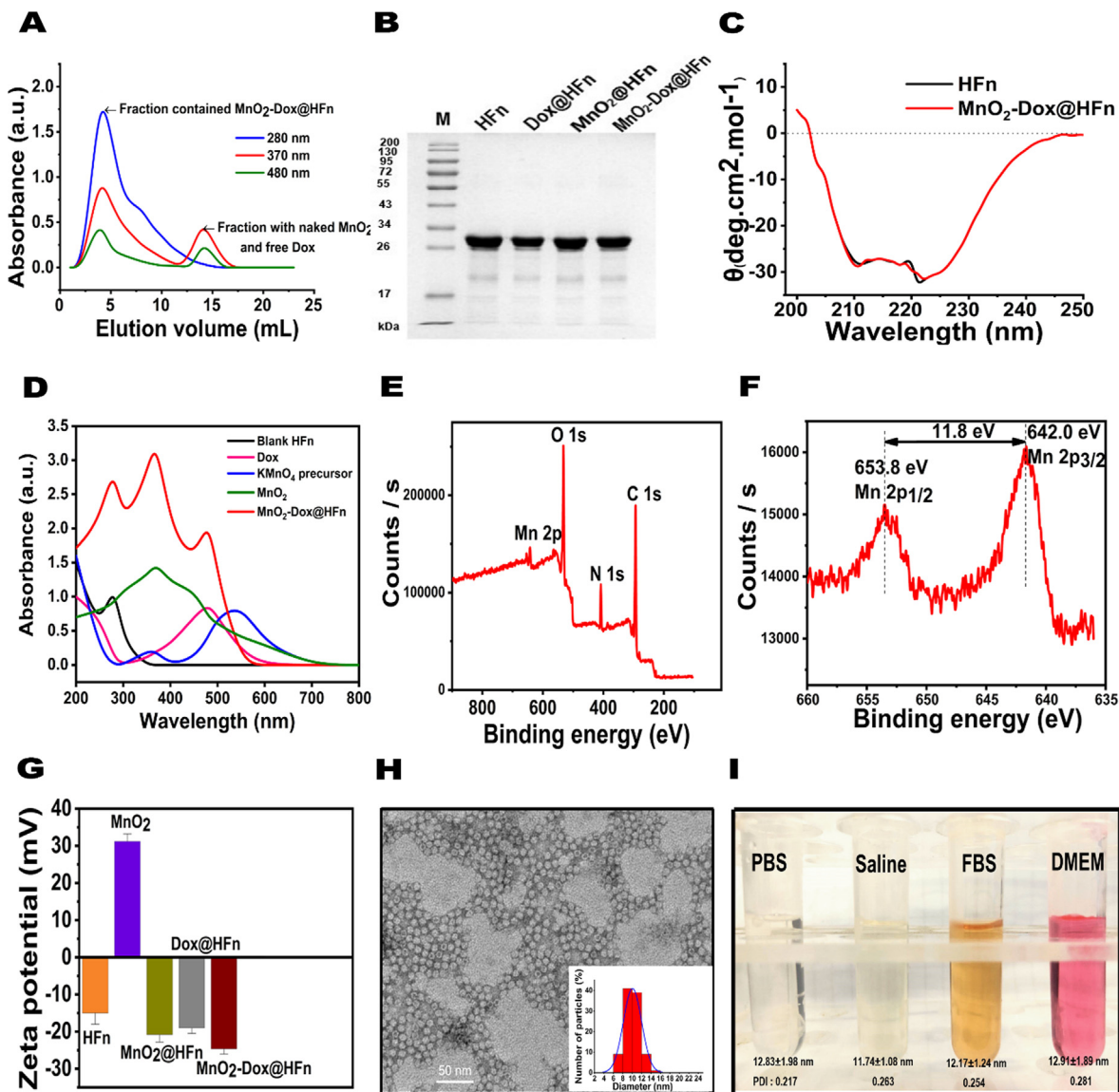
Fig. 1. Characterization of MnO$_2$-Dox@HFn. (A) Size-exclusion chromatography of MnO$_2$-Dox@HFn. The elution profile was obtained by the absorption recorded at 280, 370, and 480 nm, indicating the presence of HFn protein, MnO$_2$, and Dox, respectively. (B) SDS-PAGE protein analysis of various formulations. (C) Circular dichroism spectra of HFn and MnO$_2$-Dox@HFn with the two characteristics minima of α-helical protein around 210 nm and 221 nm. (D) UV spectra for MnO$_2$-Dox@HFn synthesis. (E) XPS analysis of MnO$_2$-Dox@HFn full scan and (F) Mn 2p core-level spectra. (G) Zeta potential of various formulations. (H) TEM image of MnO$_2$-Dox@HFn negatively stained with uranyl acetate. Inset represents the TEM size distribution. (I) Optical image of MnO$_2$-Dox@HFn dispersed in PBS, saline, FBS, and DMEM solutions with hydrodynamic particle size and polydispersity values.

bles were macroscopically observed in the acidic H$_2$O$_2$ solution after incubation with MnO$_2$-Dox@HFn as seen in Fig. 2D, vividly demonstrating the strong ability of MnO$_2$-Dox@HFn to generate O$_2$. This powerful O$_2$ generation could be explained by the equation in **S10-A, B** where both the catalytic activity and the redox reaction of MnO$_2$-Dox@HFn are conspicuous.

On the other hand, the second enzymatic activity of MnO$_2$-Dox@HFn was evaluated by the catalytic oxidation of TMB substrate in a tumor-mimicking microenvironment. As illustrated in Fig. 2E, MnO$_2$-Dox@HFn functioned as an excellent peroxidase mimetic material by developing a blue color product with maximum absorption at 652 nm, typical of the oxidized TMB. This result was validated by the equation in **S10-C**. Moreover, the real-time change in the substrate TMB absorption was monitored under different concentrations of H$_2$O$_2$ (**S11**), from which the time-course absorbance of oxidized TMB was collected (Fig. 2F). The peroxidase

kinetic parameters were plotted according to the Michaelis-Menten curve (Fig. 2G) following the equation

$$Vo = Vmax \times \frac{[S]}{(Km + [S])}$$

where V$_0$ is the initial velocity, V$_{max}$ is the maximal reaction velocity, [S] is the concentration of substrate and K$_m$ is the Michaelis constant. From the Lineweaver-Burk plot (Fig. 2H), K$_m$ and V$_{max}$ of MnO$_2$-Dox@HFn were calculated to be 28.87 $\times$ 10^{-6} M s^{-1} and 5.23 mM, respectively. As illustrated in the equation **S10-C**, the peroxidase ability of MnO$_2$-Dox@HFn catalyze the endogenous H$_2$O$_2$ to produce hydroxyl radical, a kind of reactive oxygen species, thereby leading to intracellular oxidative damage [12] which could increase the anti-tumor activity of MnO$_2$-Dox@HFn.
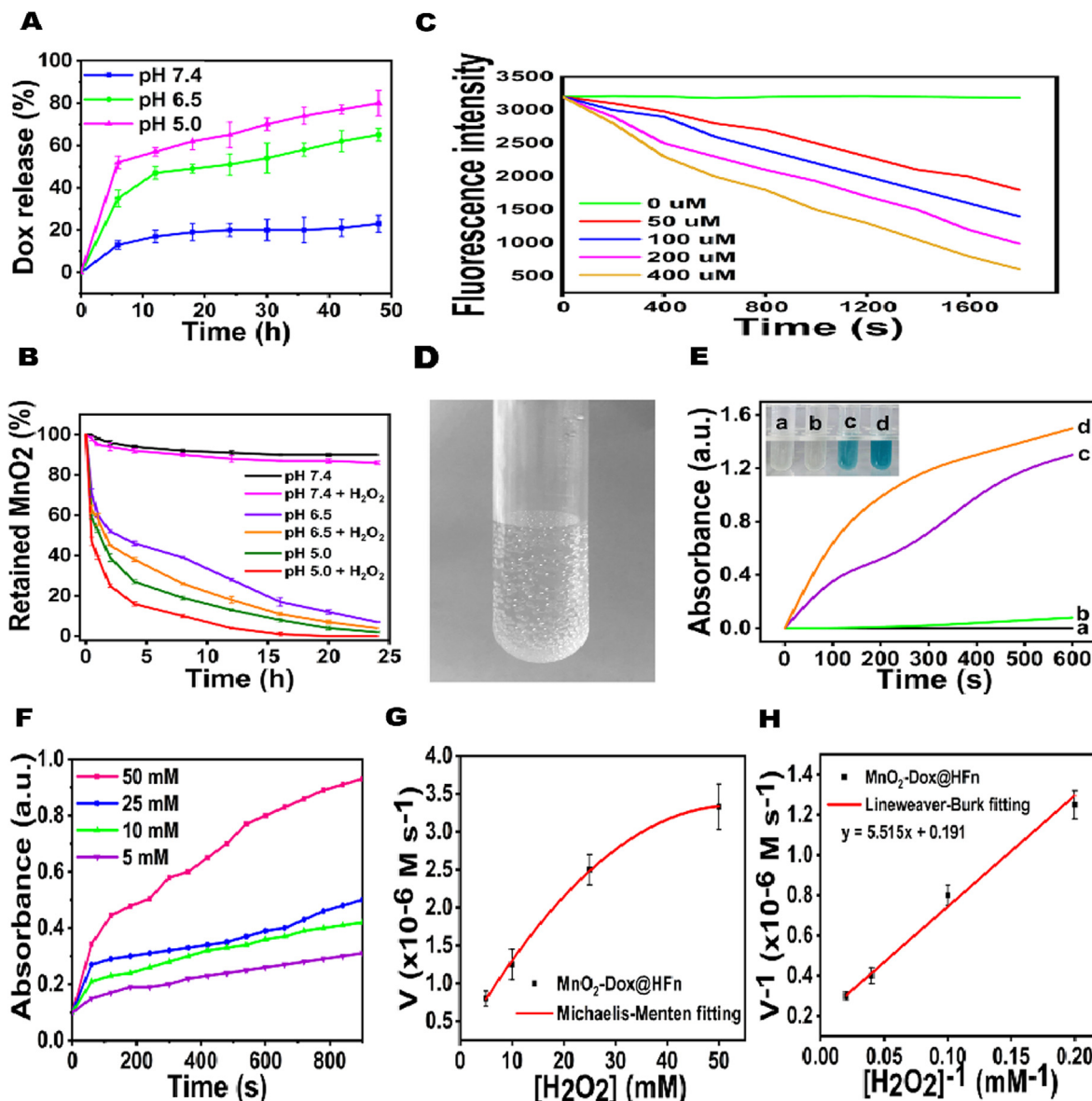
Fig. 2. Disassociation behavior of MnO₂-Dox@HFn. (A) The release profile of Dox from MnO₂-Dox@HFn at different pH. (B) MnO₂ decomposition quantified by Mn concentration using AAS. (C) O₂ generation from varied concentrations of MnO₂-Dox@HFn. [Ru(dpp)3]Cl₂ fluorescence was quenched by the O₂ generated from MnO₂-Dox@HFn. (D) O₂ bubbles were observed after incubation of MnO₂-Dox@HFn in a tumor mimic microenvironment condition. (E) Peroxidase-like activity of MnO₂-Dox@HFn measuring by the absorbance of oxidized TMB at 652 nm in the following solutions a: TMB + H₂O₂; b: TMB + MnO₂-Dox@HFn; c: TMB + H₂O₂ + MnO₂@HFn; d: TMB + H₂O₂ + MnO₂-Dox@HFn. The inset is a photograph of colored products. (F) TMB derived oxidation products overtime. (G) Michaelis-Menten and (H) Lineweaver-Burk fitting. The error bars represent the SD for three measurements.

In vitro MRI and cell viability

Taking advantage of the produced Mn^{2+} ions, which is an excellent T1-shortening agent, MRI *in vitro* study was embarked. The obvious concentration-based brightening effect in T1-weighted MR images of MnO₂-Dox@HFn at pH 6.0 was observed with a high relaxivity r1 of 33.40 mM s^{-1} (Fig. 3A-B). In contrast, no signal was found under pH 7.4, which may be attributed to the non-dissociation of MnO₂-Dox@HFn in physiological conditions.

Next, the non-toxicity of the blank nanocarrier was studied via MTT assay after 48 h incubation. As shown in Fig. 3C, cell viability remained above 90% even after incubation with concentrated HFn protein (2.5 mg mL^{-1}). The nanoformulation cell death effect in a normal environment was evaluated towards HeLa, 4 T1 and SKOV3 cells as shown in **S12**. MnO₂-Dox@HFn nanomaterial exhibited unsatisfactory effects of cytotoxicity under normoxia. Compara-

tively, the cell viability effect of MnO₂-Dox@HFn in the cancer cells under hypoxic conditions showed apparent dose-dependent anti-tumor activity (Fig. 3D-F). Intriguingly, MnO₂-Dox@HFn nanozyme demonstrated higher cytotoxicity on HeLa and 4 T1 cancer cells compared to the naked Dox. This enhancement could be attributed to a great cellular uptake of the encapsulated drug, improving its accumulation and anti-cancer efficiency. Furthermore, IC$_{50}$ of HeLa cells treated with MnO₂-Dox@HFn was 5-fold lower than the SKOV3 cells (Fig. 3G) due to the difference of TfR1 expression on their surface [42,43] allowing the cellular internalization of MnO₂-Dox@HFn. Indeed, both Dox@HFn and MnO₂-Dox@HFn possessed TfR1-targeting ligand to enter the cells. However, it is well-known that cancer hypoxia induces drug resistance, therefore the difference in cytotoxicity result between Dox@HFn and MnO₂-Dox@HFn could be explained by the increased efficiency of Dox since the unfavorable hypoxia condition was relieved and also
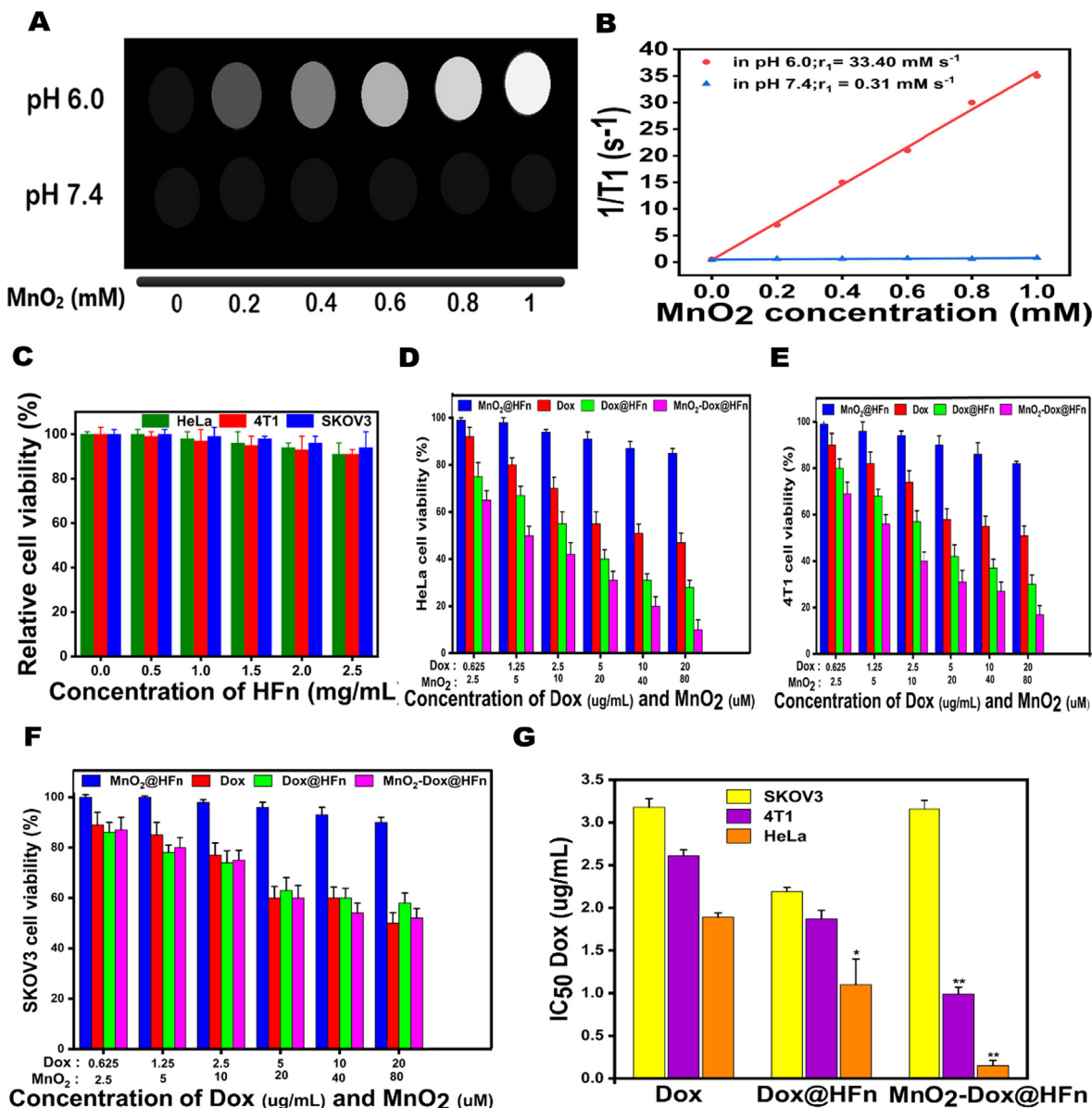
Fig. 3. *In vitro* study. (A) T1-weighted MRI *in vitro* with various MnO_2 concentrations under pH 6.0 and pH 7.4. (B) Concentration-dependent longitudinal relaxation time T1, based on readings from A. (C) Cytotoxicity of HFn carrier toward HeLa, 4 T1, and SKOV3 cancer cells. (D-F) Cell viability of three cell lines under hypoxic conditions determined by MTT assay exposed to various concentrations of nanomaterials for 48 h. The Dox concentration axis represents the quantity of Dox in each group for Dox contained formulations as well as the MnO_2 concentration axis for MnO_2 contained nanomaterials. (G) IC_{50} values of various cancer cells based on Dox concentration (*$p < 0.05$, **$p < 0.01$ vs SKOV3). Data are presented as means ± SD (n = 3).

due to the cellular damage caused by free radical produced by MnO_2.

Cellular binding of MnO_2-Dox@HFn

The quantitative cellular uptake of MnO_2-Dox@HFn was performed by flow cytometry after successfully labeled the nanozyme with FAM fluorescent probe (**S13**). To confirm whether TfR1 receptors mediate the binding of MnO_2-Dox@HFn toward cancer cells, cellular uptake was quantified in high TfR1-expressing HeLa cells and low TfR1-expressing SKOV3 cells [42,43]. As the incubation time increased, the cellular internalization was greatly increased (Fig. 4A-B), meanwhile, MnO_2-Dox@HFn carried a time-dependent cellular uptake. Significantly, MnO_2-Dox@HFn exhibited high cellular uptake potentials in HeLa cells compared to SKOV3 cells (Fig. 4C), showing that the internalization process

was mediated by TfR1 affinity. Additionally, the effect of temperature on cellular uptake at 37 °C and 4 °C has been studied, as low temperatures may inhibit the activity of cell transport proteins. As illustrated in Fig. 4D and E, the mean fluorescence intensity (MFI) at 37 °C was significantly higher than that at 4 °C. This data suggested that the uptake of MnO_2-Dox@HFn possibly involving transport proteins, which may be related to energy-dependent processes [44]. To elucidate the absorption mechanism of MnO_2-Dox@HFn, cells were pretreated with sodium azide, chlorpromazine, genistein, and amiloride to inhibit energy-dependent endocytosis, clathrin-mediated endocytosis, caveolae-mediated endocytosis, and macropinocytosis, respectively [35]. As seen in Fig. 4D and E, the presence of sodium azide remarkably reduced the cellular uptake of MnO_2-Dox@HFn, indicating an energy-dependent mechanism. Chlorpromazine pretreatment also resulted in a significant MFI decrease of MnO_2-Dox@HFn uptake,
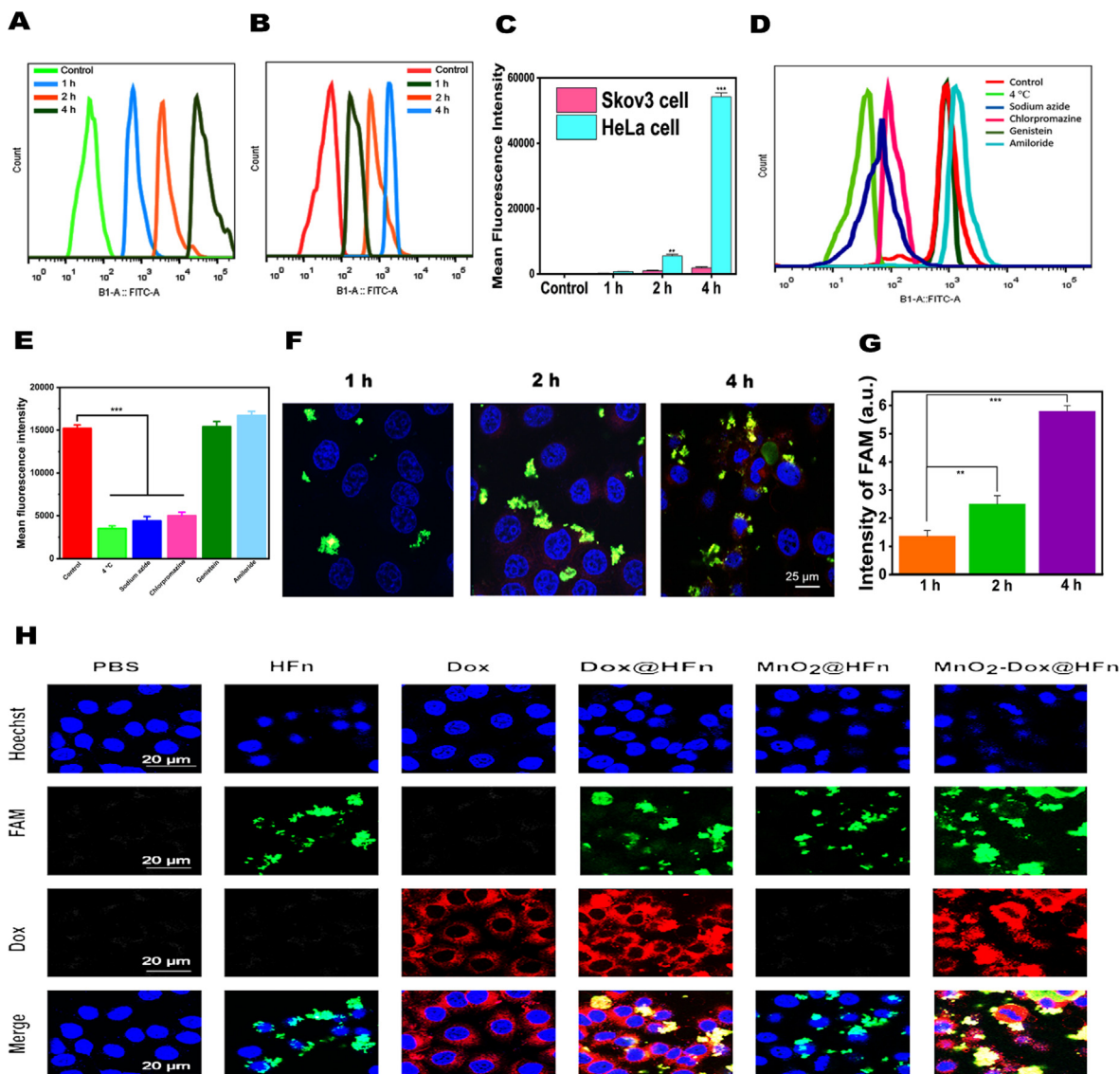
Fig. 4. Flow cytometry analysis of the cellular uptake of FAM-MnO$_2$-Dox@HFn in (A) HeLa and (B) SKOV3 cancer cells. (C) Quantitative analysis of FAM-MnO$_2$-Dox@HFn binding according to A and B. (D) Cellular uptake of FAM-MnO$_2$-Dox@HFn by flow cytometry in HeLa cells incubated with various endocytosis inhibitors. (E) The relative fluorescent intensity of FAM-MnO$_2$-Dox@HFn with the selective inhibitors according to D (**p < 0.01, ***p < 0.001 vs control) (n = 3). (F) Internalization of FAM-MnO$_2$-Dox@HFn in HeLa cells after incubation for 1, 2 and 4 h via CLSM. The nucleus was stained with Hoechst 33,342 (blue). The uptake of nanozyme was visualized by HFn protein carrier labeled with FAM (green) and the red fluorescence of Dox. (G) Quantitative analysis of FAM intensity according to D using ImageJ software (**p < 0.01, ***p < 0.001 vs 1 h). (H) HeLa cells uptake of various nanomaterials after 4 h incubation visualized by CLSM.

suggesting that the cell entry pathway was mainly involved in receptor- and clathrin-mediated endocytosis. Besides, pretreatment of the cells with genistein and amiloride did not affect the uptake of MnO$_2$-Dox@HFn nanomaterials. Based on these findings, we suggest that MnO$_2$-Dox@HFn are mainly bound with TfR1 receptors and entering cells by TfR1 clathrin-mediated endocytosis. Subsequently, the co-localization study of MnO$_2$-Dox@HFn using CLSM displayed an obvious cellular internalization trend over time (Fig. 4F-G), which demonstrated the nuclear translocation of the nanozyme. The accumulation of Dox fluorescence released from MnO$_2$-Dox@HFn inside the cell nuclei was observed (Fig. 4H), which was stronger than the naked Dox. It demonstrates that the specific binding of HFn nanocage through the TfR1-mediated endocytosis enhanced cellular drug accumulation compared to the passive diffusion performed by free Dox. Indeed, these results can explain the enhanced anti-tumor efficiency of MnO$_2$-Dox@HFn nanozyme.

Cellular oxygen generation

As stated previously, hypoxia has serious consequences in tumor progression, hence the intracellular oxygenation of MnO$_2$-Dox@HFn was examined. The cellular O$_2$ level was assessed by [Ru(dpp)3]Cl$_2$ probe, which decreases its luminescence intensity when the O$_2$ content increase [45]. As obviously illustrated in Fig. 5A-B, MnO$_2$-Dox@HFn triggered the generation of in situ O$_2$ and the hypoxic environment was completely removed after 24 h incubation. To further confirm such findings, the expression of O$_2$-regulated HIF-1α protein was quantified after inducing severe hypoxia with CoCl$_2$. Interestingly, the HIF-1α expression level of cells treated with MnO$_2$-Dox@HFn was significantly down-regulated (Fig. 5C-D), while for the control and Dox@HFn treated, cells were still under hypoxic challenge. Cells contain very little amount of HIF-1α when O$_2$ levels are high, hence this result con-
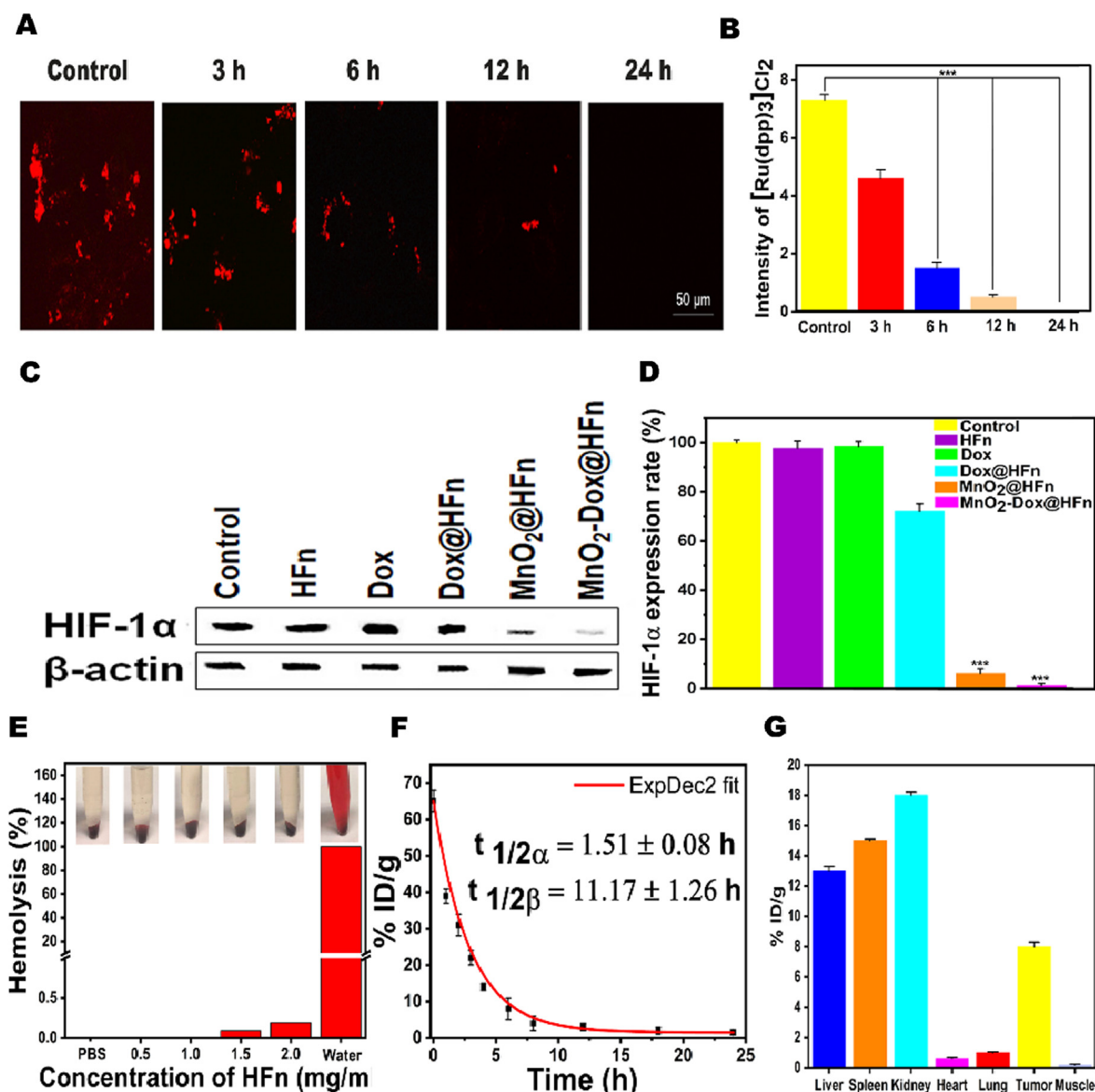
Fig. 5. (A) Intracellular hypoxia assessed by [Ru(dpp)3]Cl$_2$ fluorescence probe at different incubation times of MnO$_2$-Dox@HFn. (B) Quantitative evaluation of fluorescence intensity according to A (***p < 0.001 vs control). (C) Western blot analysis of HIF-1α expression in HeLa cells under different treatments. β-actin was used as a loading control. (D) Quantitative detection of HIF-1α based on C (***p < 0.001 vs control). (E) Hemolytic activity of MnO$_2$-Dox@HFn using PBS as reference and water as a 100% hemolysis value. (F) Blood circulation curve of MnO$_2$-Dox@HFn based on Mn quantification by AAS. (G) Tissue biodistribution of MnO$_2$-Dox@HFn in mice after intravenous injection.

firmed that MnO$_2$-Dox@HFn nanozyme successfully alleviates the hypoxia status of cancer cells.

Hemocompatibility, pharmacokinetic and biodistribution evaluation in vivo

To determinate the potential toxicity of MnO$_2$-Dox@HFn during systemic circulation for *in vivo* study, hemolysis behavior was first investigated. No obvious hemolytic effect was observed even at the highest concentration of MnO$_2$-Dox@HFn (2 mg mL^{-1}) as does PBS (Fig. 5E), confirming the good hemocompatibility of MnO$_2$-Dox@HFn. Then, the blood circulation of MnO$_2$-Dox@HFn was analyzed in healthy mice by measuring the concentration of Mn in the body via AAS. The concentration of MnO$_2$-Dox@HFn decreased over time following the two-compartment model with circulating half-lives of $t_{1/2\alpha}$ = 1.51 ± 0.08 h and $t_{1/2\beta}$ = 11. 17 ± 1.26 h (Fig. 5F). This long circulation time of MnO$_2$-Dox@HFn in the blood allows them

to accumulate in the tumor site via the EPR effect. To confirm this hypothesis, the tissue biodistribution of MnO$_2$-Dox@HFn was examined. As can be seen in Fig. 5G, a high Mn level in the tumor tissue and kidneys was found, indicating that MnO$_2$-Dox@HFn was accumulated in the tumor region and excreted with renal clearance.

In vivo tumor imaging by MRI

To demonstrate the tumor-specific selectivity of MnO$_2$-Dox@HFn as a potent MRI T1-shortening agent, the nanomaterial was injected intratumorally and also into the muscle tissue on the opposite side. A remarkable brighter appearance was observed in the tumor region after only 20 min post-injection (Fig. 6A), the time for the nanozyme shell to dissociate, permitting real-time evaluation of the tumor. However, the non-tumor area with the same dose of MnO$_2$-Dox@HFn injected did not show any obvious
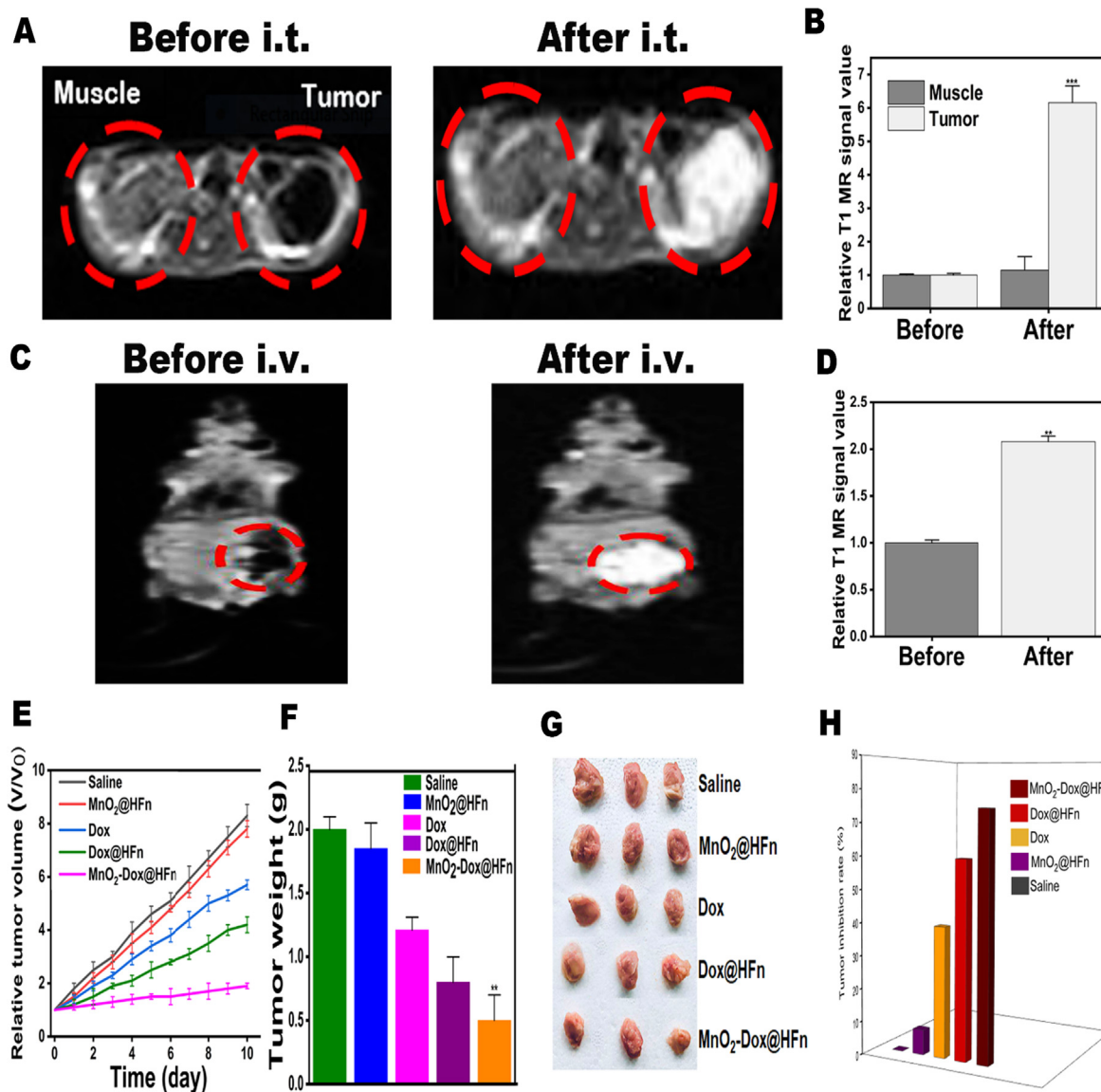
Fig. 6. T1-MR images of 4 T1 tumor-bearing mice through (A) local and (C) intravenous injection of MnO$_2$-Dox@HFn. (B) and (D) Quantification of T1-MRI signals via intratumorally and intravenously injection according to A and C, respectively (n = 3; **p < 0.01, ***p < 0.001 vs before). (E) Tumor growth in various treated groups (n = 3). (F) Tumor weight at the endpoint of the study (**p < 0.01). (G) Representative tumor images were harvested from mice after the treatment. (H) Tumor growth inhibition rate.

T1 signal (Fig. 6B). This result demonstrated the selective delivery of MnO$_2$-Dox@HFn within cancer tissues only, leaving normal tissue unharmed. Consecutively, after 6 h post-intravenous injection of MnO$_2$-Dox@HFn, the tumor site was strongly illuminated (Fig. 6-C-D), further indicating its precise tumor distinction and cancer accumulation.

In vivo study for Anti- tumor activity

Having proved the specific tumor-targeting ability of MnO$_2$-Dox@HFn, their potential *in vivo* anti-tumor activity was studied. The variation trend of tumor volume during the treatment is shown in Fig. 6E. According to the tumor weight and photographs of tumor tissues excised after the treatment (Fig. 6F-G), MnO$_2$-Dox@HFn treated group showed the greatest therapeutic activity with the highest tumor inhibition rate of 78.5% (Fig. 6H). The enhancement anti-tumor ability of MnO$_2$-Dox@HFn compared to Dox@HFn could be explained by the effect of MnO$_2$ to relieve tumor hypoxia. Since the chemotherapeutic activity of Dox has been demonstrated to be less effective under hypoxic rather than

in normoxic environment [46,47]. Additionally, the antitumor efficacy was detected by TUNEL assay and H&E staining. The results are consistent with the *in vitro* study, which shows the unsatisfied tumor cell killing capacity of free Dox, and improved when encapsulated within the HFn nanocage (Dox@HFn) for the tumor-targeting delivery (Fig. 7A). Besides, the weak anti-tumor ability of MnO$_2$@HFn could be explained by the free radicals produced from MnO$_2$, leading to cancer cell damage. Contrarily, an obvious cell apoptosis signal was noticed in the tumor tissue treated with MnO$_2$-Dox@HFn nanozyme. Below, the histological analysis after H&E staining from MnO$_2$-Dox@HFn-treated mice showed their potentiality to suppress tumor growth. The ability of MnO$_2$-Dox@HFn to regulate hypoxic conditions in tumor tissue was also evaluated through immunohistochemistry of HIF-1α and Ki-67. MnO$_2$-Dox@HFn-treated mice decreased until 91.06% the expression of HIF-1α as compared with the saline group (Fig. 7B), due to their *in vivo* tumor oxygenation ability. Benefiting from this down-regulation of HIF-1α protein, cell migration was inhibited as proved by the suppression of Ki-67 proliferative cells in the MnO$_2$-Dox@HFn group, showing remarkable interest to prevent
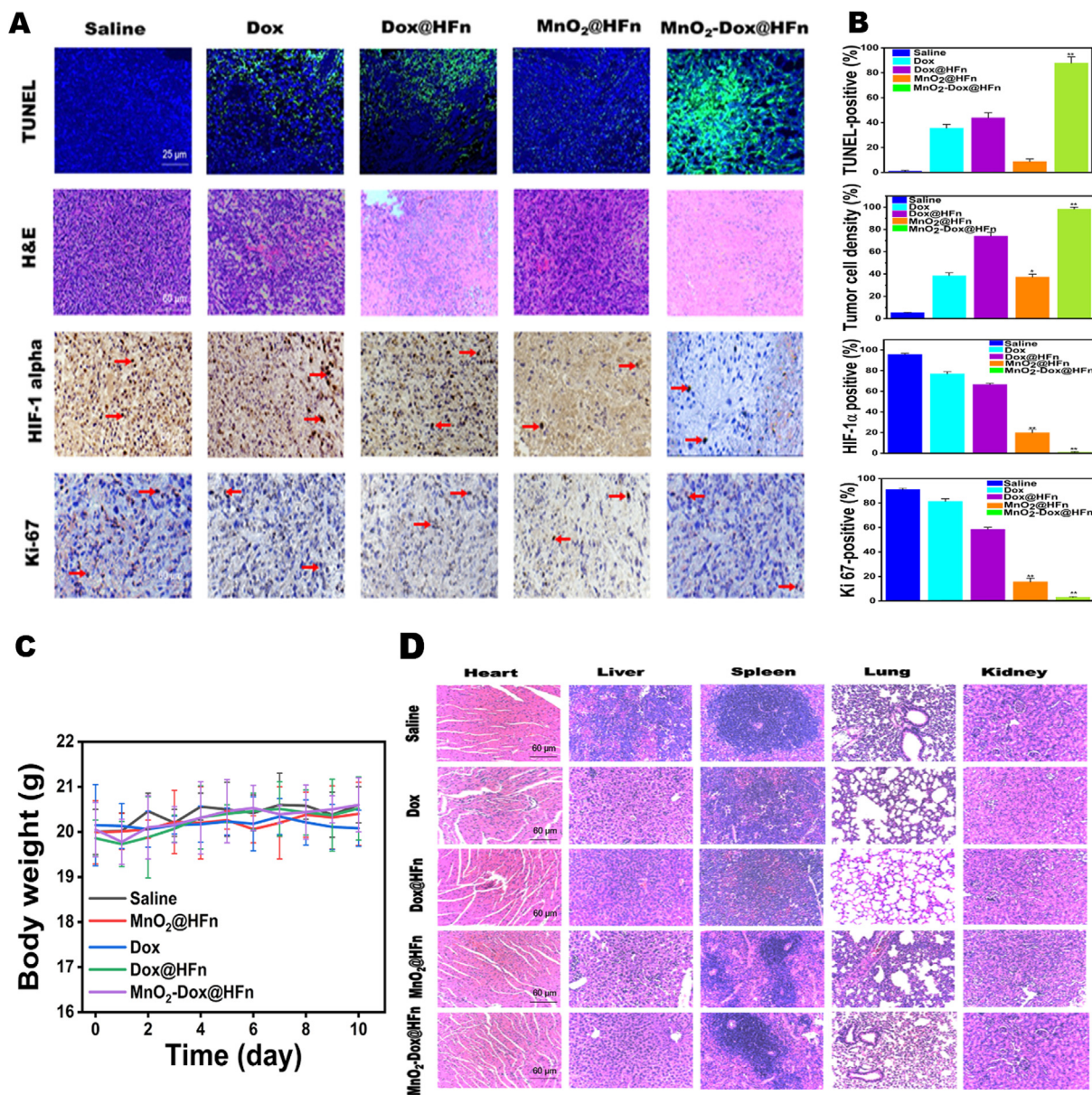
Fig. 7. Histological study and biosafety. (A) Immunofluorescence analysis of the resected tumor tissues. TUNEL assays evaluating apoptotic cells where nuclei were stained blue (DAPI staining), and apoptotic cells were stained green (TUNEL staining). H&E staining assay. Immunohistochemical staining of HIF-1α and Ki-67 (brown-stained cells). (B) Quantification of the positive cell rate in the TUNEL apoptosis; H&E; HIF-1α and Ki-67 staining (n = 3; **p < 0.01 or *p < 0.05 vs free Dox). (C) Body weight during the whole treatment. (D) H&E staining of major organs tissue sections.

tumor metastasis. Taken together, the expected duration of a single dose therapeutic effect of MnO_2-Dox@HFn might be around 48 h as deducted from the *in vitro* cytotoxicity study. The cellular oxygen generation also demonstrated that after 24 h incubation with MnO_2-Dox@HFn, the hypoxia was completely relieved; as well as confirmed the western blot analysis during which the HIF-1α expression level of cells treated with MnO_2-Dox@HFn for 48 h was significantly down-regulated. Further proved with the *in vivo* study, while the mouse was treated with MnO_2-Dox@HFn every 2 days during the treatment period and significant therapeutic activity was observed.

Biosafety

Finally, the biosafety of MnO_2-Dox@HFn was evaluated through the body weight and the H&E staining of major organs. As shown in Fig. 7C, there were no significant changes in the body weight in all

tested groups. Likewise, based on the histological H&E analysis, no noticeable toxicity nor abnormality was observed in all of the groups after the whole therapeutic period (Fig. 7D). These results engaged the excellent biocompatibility and good safety profile of MnO_2-Dox@HFn.

Conclusions

In summary, the MnO_2-Dox@HFn nanozyme was formulated in a facile manner through pH change. Compared to other approaches, this study highlights several important concepts that may promote the exploration of theranostic nanozyme for cancer therapy. First, MnO_2-Dox@HFn showed peroxidase and catalase-like activity to generate superior O_2 indispensable to overcome tumor hypoxia. Secondly, the nanozyme provides tumor-specific MR imaging-guided cancer treatment. Thirdly, MnO_2-Dox@HFn exhibited potential anti-cancer ability, which could be attributed

to the intracellular oxidase damage from peroxidase-activity and the chemotherapeutic effect of Dox. Lastly, MnO_2-Dox@HFn reduces malignant cell proliferation *in vivo*, which is beneficial for clinical tumor therapy.

Compliance with Ethics Requirements

Animal study Ethics statement: All experiments involving animals were conducted according to the ethical policies and regulations provided by the Guide for Care and Use of Laboratory Animals, approved by China Pharmaceutical University (Approval no. 2019-1205).

CRediT authorship contribution statement

Hanitrarimalala Veroniaina: Conceptualization, Methodology, Software, Data curation, Writing - original draft. **Zhenghong Wu:** Supervision, Visualization, Investigation. **Xiaole Qi:** Supervision, Validation, Writing - review & editing.

Declaration of Competing Interest

The authors declare that they have no known competing financial interests or personal relationships that could have appeared to influence the work reported in this paper.

Appendix A. Supplementary material

Supplementary data to this article can be found online at https://doi.org/10.1016/j.jare.2021.02.004.

References

[1] Chang CH, Qiu J, O'Sullivan D, Buck MD, Noguchi T, Curtis JD, et al. Metabolic competition in the tumor microenvironment is a driver of cancer progression. Cell 2015;162:1229–41.

[2] Corbet C, Feron O. Tumour acidosis: From the passenger to the driver's seat. Nat Rev Cancer 2017;17:577–93.

[3] Mura S, Nicolas J, Couvreur P. Stimuli-responsive nanocarriers for drug delivery. Nat Mater 2013;12:991–1003.

[4] Allinen M, Beroukhim R, Cai L, Brennan C, Lahti-Domenici J, Huang H, et al. Molecular characterization of the tumor microenvironment in breast cancer. Cancer Cell 2004;6:17–32.

[5] Guo SY, Sun D, Ni DL, Yu MR, Qian K, Zhang W, et al. Smart tumor microenvironment-responsive nanotheranostic agent for effective cancer therapy. Adv Funct Mater 2020:2000486.

[6] Bertout JA, Patel SA, Simon MC. The impact of o 2 availability on human cancer. Nat Rev Cancer 2008;8:967–75.

[7] Quail DF, Joyce JA. Microenvironmental regulation of tumor progression and metastasis. Nat Med 2013;19:1423.

[8] Jiang W, Li Q, Xiao L, Dou J, Liu Y, Yu W, et al. Hierarchical multiplexing nanodroplets for imaging-guided cancer radiotherapy via DNA damage enhancement and concomitant DNA repair prevention. ACS Nano 2018;12:5684–98.

[9] Meng Z, Zhou X, Xu J, Han X, Dong Z, Wang H, et al. Light-triggered in situ gelation to enable robust photodynamic-immunotherapy by repeated stimulations. Adv Mater 2019;31:1900927.

[10] Zhang Y, Bo S, Feng T, Qin X, Wan Y, Jiang S, et al. A versatile theranostic nanoemulsion for architecture-dependent multimodal imaging and dually augmented photodynamic therapy. Adv Mater 2019;31:1806444.

[11] Chen Q, Feng L, Liu J, Zhu W, Dong Z, Wu Y, et al. Intelligent albumin–mno2 nanoparticles as ph-/h2o2-responsive dissociable nanocarriers to modulate tumor hypoxia for effective combination therapy. Adv Mater 2016;28:7129–36.

[12] Wang Z, Zhang Y, Ju E, Liu Z, Cao F, Chen Z, et al. Biomimetic nanoflowers by self-assembly of nanozymes to induce intracellular oxidative damage against hypoxic tumors. Nat Commun 2018;9:1–14.

[13] Yang G, Xu L, Chao Y, Xu J, Sun X, Wu Y, et al. Hollow mno 2 as a tumor-microenvironment-responsive biodegradable nano-platform for combination therapy favoring antitumor immune responses. Nat Commun 2017;8:1–13.

[14] Fan W, Bu W, Shen B, He Q, Cui Z, Liu Y, et al. Intelligent mno2 nanosheets anchored with upconversion nanoprobes for concurrent ph-/h2o2-responsive ucl imaging and oxygen-elevated synergetic therapy. Adv Mater 2015;27:4155–61.

[15] Zhu P, Chen Y, Shi J. Nanoenzyme-augmented cancer sonodynamic therapy by catalytic tumor oxygenation. ACS Nano 2018;12:3780–95.

[16] Zhu W, Dong Z, Fu T, Liu J, Chen Q, Li Y, et al. Modulation of hypoxia in solid tumor microenvironment with mno2 nanoparticles to enhance photodynamic therapy. Adv Funct Mater 2016;26:5490–8.

[17] Song M, Liu T, Shi C, Zhang X, Chen X. Bioconjugated manganese dioxide nanoparticles enhance chemotherapy response by priming tumor-associated macrophages toward m1-like phenotype and attenuating tumor hypoxia. ACS Nano 2016;10:633–47.

[18] Zhao Z, Fan H, Zhou G, Bai H, Liang H, Wang R, et al. Activatable fluorescence/ mri bimodal platform for tumor cell imaging via mno2 nanosheet–aptamer nanoprobe. J Am Chem Soc 2014;136:11220–3.

[19] Lee N, Hyeon T. Designed synthesis of uniformly sized iron oxide nanoparticles for efficient magnetic resonance imaging contrast agents. Chem Soc Rev 2012;41:2575–89.

[20] Chung C-H, Lu K-Y, Lee W-C, Hsu W-J, Lee W-F, Dai J-Z, et al. Fucoidan-based, tumor-activated nanoplatform for overcoming hypoxia and enhancing photodynamic therapy and antitumor immunity. Biomaterials 2020;257:120227.

[21] Zhang Y-H, Qiu W-X, Zhang M, Zhang L, Zhang X-Z. Mno2 motor: A prospective cancer-starving therapy promoter. ACS Appl Mater Interfaces 2018;10:15030–9.

[22] He Q, Hu H, Zhang Q, Wu T, Zhang Y, Li K, et al. Ultra-dispersed biomimetic nanoplatform fabricated by controlled etching agglomerated mno2 for enhanced photodynamic therapy and immune activation. Chem Eng J 2020;397:125478.

[23] Zhang L, Yang Z, Ren J, Ba L, He W, Wong C-Y. Multifunctional oxygen-enriching nano-theranostics for cancer-specific magnetic resonance imaging and enhanced photodynamic/photothermal therapy. Nano Res 2020;13:1389–98.

[24] Liang R, Wei M, Evans DG, Duan X. Inorganic nanomaterials for bioimaging, targeted drug delivery and therapeutics. Chem Commun 2014;50:14071–81.

[25] Cai Y, Wang Y, Zhang T, Pan Y. Gadolinium-labeled ferritin nanoparticles as t1 contrast agents for magnetic resonance imaging of tumors. ACS Appl Nano Mater 2020;3:8771–83.

[26] Von Maltzahn G, Park J-H, Lin KY, Singh N, Schwöppe C, Mesters R, et al. Nanoparticles that communicate in vivo to amplify tumour targeting. Nat Mater 2011;10:545–52.

[27] Zhang S, Zang J, Chen H, Li M, Xu C, Zhao G. The size flexibility of ferritin nanocage opens a new way to prepare nanomaterials. Small 2017;13:1701045.

[28] Theil EC. Ferritin: Structure, gene regulation, and cellular function in animals, plants, and microorganisms. Annu Rev Biochem 1987;56:289–315.

[29] Cheng X, Fan K, Wang L, Ying X, Sanders AJ, Guo T, et al. Tfr1 binding with h-ferritin nanocarrier achieves prognostic diagnosis and enhances the therapeutic efficacy in clinical gastric cancer. Cell Death Dis 2020;11. 92–92.

[30] Li L, Fang CJ, Ryan JC, Niemi EC, Lebrón JA, Björkman PJ, et al. Binding and uptake of h-ferritin are mediated by human transferrin receptor-1. Proc Natl Acad Sci 2010;107:3505–10.

[31] Quan C-Y, Chen J-X, Wang H-Y, Li C, Chang C, Zhang X-Z, et al. Core− shell nanosized assemblies mediated by the α− β cyclodextrin dimer with a tumor-triggered targeting property. ACS Nano 2010;4:4211–9.

[32] Fan K, Cao C, Pan Y, Lu D, Yang D, Feng J, et al. Magnetoferritin nanoparticles for targeting and visualizing tumour tissues. Nat Nanotechnol 2012;7:459–64.

[33] Huang Y, Ren J, Qu X. Nanozymes: Classification, catalytic mechanisms, activity regulation, and applications. Chem Rev 2019;119:4357–412.

[34] Huang H, Sha K, Veroniaina H, Wu Z, Wu Z, Qi X. Ca 2+ participating self-assembly of an apoferritin nanostructure for nucleic acid drug delivery. Nanoscale 2020.

[35] Ji P, Huang H, Yuan S, Wang L, Wang S, Chen Y, et al. Ros-mediated apoptosis and anticancer effect achieved by artesunate and auxiliary fe (ii) released from ferriferous oxide-containing recombinant apoferritin. Adv Healthcare Mater 2019;8:1900911.

[36] Dai M, Cui P, Yu M, Han J, Li H, Xiu R. Melatonin modulates the expression of vegf and hif-1α induced by cocl2 in cultured cancer cells. J Pineal Res 2008;44:121–6.

[37] Li L, Muñoz-Culla M, Carmona U, Lopez MP, Yang F, Trigueros C, et al. Ferritin-mediated sirna delivery and gene silencing in human tumor and primary cells. Biomaterials 2016;98:143–51.

[38] Fan H-L, Ran F, Zhang X-X, Song H-M, Niu X-Q, Kong L-B, et al. Hollow carbon microspheres/mno 2 nanosheets composites: Hydrothermal synthesis and electrochemical behaviors. Nano-Micro Lett 2015;7:59–67.

[39] Ghaffari S-B, Sarrafzadeh M-H, Fakhroueian Z, Khorramizadeh MR. Flower-like curcumin-loaded folic acid-conjugated zno-mpa-βcyclodextrin nanostructures enhanced anticancer activity and cellular uptake of curcumin in breast cancer cells. Mater Sci Eng, C 2019;103:109827.

[40] Cheng Q, Li Z-H, Sun Y-X, Zhang X-Z. Controlled synthesis of a core-shell nanohybrid for effective multimodal image-guided combined photothermal/ photodynamic therapy of tumors. NPG Asia Mater 2019;11:63.

[41] Liu Y, Zhen W, Jin L, Zhang S, Sun G, Zhang T, et al. All-in-one theranostic nanoagent with enhanced reactive oxygen species generation and modulating tumor microenvironment ability for effective tumor eradication. ACS Nano 2018;12:4886–93.

[42] Daniels TR, Bernabeu E, Rodríguez JA, Patel S, Kozman M, Chiappetta DA, et al. The transferrin receptor and the targeted delivery of therapeutic agents against cancer. Biochim Biophys Acta 1820;2012:291–317.

[43] Yue J, Liu S, Wang R, Hu X, Xie Z, Huang Y, et al. Transferrin-conjugated micelles: Enhanced accumulation and antitumor effect for transferrin-receptor-overexpressing cancer models. Mol Pharm 2012;9:1919–31.

[44] Chen Z, Xing L, Fan Q, Cheetham AG, Lin R, Holt B, et al. Drug-bearing supramolecular filament hydrogels as anti-inflammatory agents. Theranostics 2017;7:2003.

[45] Chen H, Tian J, He W, Guo Z. H2o2-activatable and o2-evolving nanoparticles for highly efficient and selective photodynamic therapy against hypoxic tumor cells. J Am Chem Soc 2015;137:1539–47.

[46] Sanna K, Rofstad EK. Hypoxia-induced resistance to doxorubicin and methotrexate in human melanoma cell lines in vitro. Int J Cancer 1994;58:258–62.

[47] Luk CK, Veinot-Drebot L, Tjan E, Tannock IF. Effect of transient hypoxia on sensitivity to doxorubicin in human and murine cell lines. J Natl Cancer Inst 1990;82:684–92.